JACS
JOURNAL OF THE AMERICAN CHEMICAL SOCIETY
pubs.acs.org/JACS
Article

# Mechanistic Investigation of Molybdenum Disulfide Defect Photoluminescence Quenching by Adsorbed Metallophthalocyanines

Samuel H. Amsterdam,[‡] Teodor K. Stanev,[‡] Luqing Wang, Qunfei Zhou, Shawn Irgen-Gioro, Suyog Padgaonkar, Akshay A. Murthy, Vinod K. Sangwan, Vinayak P. Dravid, Emily A. Weiss, Pierre Darancet,* Maria K. Y. Chan,* Mark C. Hersam,* Nathaniel P. Stern,* and Tobin J. Marks*

Cite This: *J. Am. Chem. Soc.* 2021, 143, 17153−17161
Read Online
ACCESS | Metrics & More | Article Recommendations | Supporting Information

**ABSTRACT:** Lattice defects play an important role in determining the optical and electrical properties of monolayer semiconductors such as $MoS_2$. Although the structures of various defects in monolayer $MoS_2$ are well studied, little is known about the nature of the fluorescent defect species and their interaction with molecular adsorbates. In this study, the quenching of the low-temperature defect photoluminescence (PL) in $MoS_2$ is investigated following the deposition of metallophthalocyanines (MPcs). The quenching is found to significantly depend on the identity of the phthalocyanine metal, with the quenching efficiency decreasing in the order CoPc > CuPc > ZnPc, and almost no quenching by metal-free $H_2$Pc is observed. Time-correlated single photon counting (TCSPC) measurements corroborate the observed trend, indicating a decrease in the defect PL lifetime upon MPc adsorption, and the gate voltage-dependent PL reveals the suppression of the defect emission even at large Fermi level shifts. Density functional theory modeling argues that the MPc complexes stabilize dark negatively charged defects over luminescent neutral defects through an electrostatic local gating effect. These results demonstrate the control of defect-based excited-state decay pathways via molecular electronic structure tuning, which has broad implications for the design of mixed-dimensional optoelectronic devices.

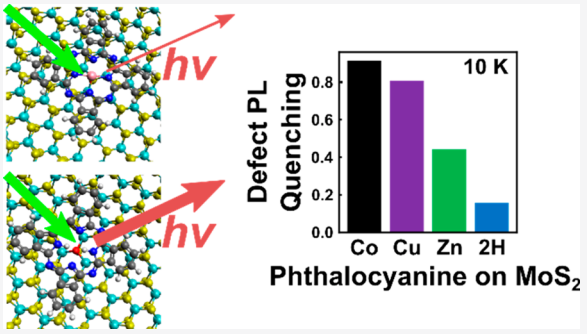


## INTRODUCTION

Transition metal dichalcogenides (TMDs) have emerged as an important class of two-dimensional (2D) semiconductors,[1] with applications as diverse as flexible electronics,[2] sensors,[3,4] photovoltaics[5] and other photonic devices,[6] neuromorphic computing,[7−9] and catalysis.[10] Among the TMDs, $MoS_2$ is the most widely studied and represents an informative model system for exploring the fundamental physics and chemistry of TMDs.[11] While $MoS_2$ has exceptional inherent optoelectronic properties, there are new opportunities in combining it with other classes of materials to form mixed-dimensional heterojunctions.[12,13] These interfaces leverage the unique properties of their constituent materials to realize new optoelectronic performance metrics, heterojunction device concepts, and emergent phenomena that are not possible in either isolated system. In this regard, the interface of molecular materials and monolayer $MoS_2$ is of particular interest due to the broad synthetic tunability, controllable assembly, and facile processing of the former as well as the exceptional optical and electrical properties of the latter.[14−16] Molecular heterojunctions have been used extensively to modulate the photoluminescence (PL) of monolayer $MoS_2$, including quenching the PL by charge transfer,[17,18] augmenting the emission via energy transfer,[19] enhancing Raman scattering,[20] and increasing the PL quantum yield (PLQY) by defect passivation.[21]

Understanding and controlling the defect-related optical response in monolayer $MoS_2$ are essential to realizing its potential in optoelectronic and quantum technologies.[22−24] Defects in $MoS_2$ play an important role in electronic transport,[25,26] doping,[27,28] and exciton recombination.[29] At low temperatures (<150 K), many defects in $MoS_2$ become luminescent, exhibiting PL at wavelengths greater than 700 nm with intensities similar to or greater than the $MoS_2$ A-exciton at 650−670 nm. While this defect PL is ubiquitous in $MoS_2$ at low temperatures,[30] the structural and chemical origins of these bright defects remain unclear.[31,32]

**Received:** July 26, 2021
**Published:** October 6, 2021







https://doi.org/10.1021/jacs.1c07795
*J. Am. Chem. Soc.* 2021, 143, 17153−17161

Since emissive defect states have been shown to be efficient single phonon emitters,[33,34] methods for modulating defect emission have potential for quantum information technologies. The broad background from the $MoS_2$ defects has a deleterious effect on the correlation score of single photon emitters that overlap spectrally.[33,34] Selective control of the emissive properties of specific defects in $MoS_2$ would be beneficial to this field. In addition, defect-bound excitons have been implicated in exciton−exciton annihilation processes that limit the PL quantum yield at high excitation powers.[35] Understanding and controlling the chemical environment of these defect-bound excitons will be essential in the application of $MoS_2$ in high-powered optoelectronic devices such as lasers.

To date, no molecular strategy has been devised to fully quench the defect PL in $MoS_2$. Encapsulation with hexagonal boron nitride (hBN) can reduce the background defect PL,[36] but implementing this strategy is labor-intensive and not scalable. Molecular approaches to $MoS_2$ defect passivation have also been explored,[37−39] but these strategies do not efficiently quench the defect PL.[29] A notable exception is zinc phthalocyanine (ZnPc), which has been shown to partially quench the defect emissions of both $MoS_2$ and $MoSe_2$.[40] Understanding the interactions of molecular adsorbates with defects in $MoS_2$ is thus essential to inform future efforts in the rational chemical modification of defect-based optoelectronic properties.

Based on theoretical predictions and experimental observations, the most common intrinsic point defect in $MoS_2$ is thought to be a sulfur vacancy ($S_{vac}$), which creates localized states near the conduction band edge (CBE).[41,42] Recent work has shown that previously undetected oxygen substitutions ($O_{sub}$) also represent a significant fraction of the point defects in $MoS_2$.[43,44] While point defects in $MoS_2$ are correlated with defect PL, there is some evidence that molecular adsorbates play a role in this emission. For example, $He^+$ bombardment creates point defects in $MoS_2$ that are associated with bright and narrow PL,[22,34] but these defects are not luminescent until they are exposed to gases.[45] Furthermore, defect emission is enhanced by exposure to water and light but not $O_2$ alone.[46] The location of the Fermi level also plays a critical role in the PLQY of $MoS_2$ defects by changing the relative electron occupancy of the midgap trap states, exciton states, trion states, and free carriers in the conduction band. For example, decreasing the gate voltage (lowering the Fermi level) in a backgate configuration increases the defect PL, while increasing the gate voltage (raising the Fermi level) suppresses it.[32] Defects and adsorbed gaseous species can also alter the doping level of $MoS_2$. For example, inducing point defects by $He^+$ bombardment as noted above[27] or heating in an ultrahigh vacuum[38] degenerately dopes $MoS_2$ in an n-type manner, whereas electron-withdrawing $O_2$ acts as a p-type dopant.[27] Defects can also interact strongly with adsorbed gases, as in the case of hydrogen.[47] Recent efforts to decouple the influence of doping and the chemical interactions of gases on the defect emission showed that adsorbed $O_2$ reduces the defect emission compared to pristine $MoS_2$, which has an equal Fermi level.[32] To extend this work and use molecular adsorbates to manipulate defect PL, a more complete understanding of the mechanism of $MoS_2$ defect PL quenching is needed.

In this study, we systematically explore the interactions of various metallophthalocyanines (MPcs; Figure 1) with defects in monolayer $MoS_2$ to better understand defect−adsorbate interactions. Metallophthalocyanines present an ideal system

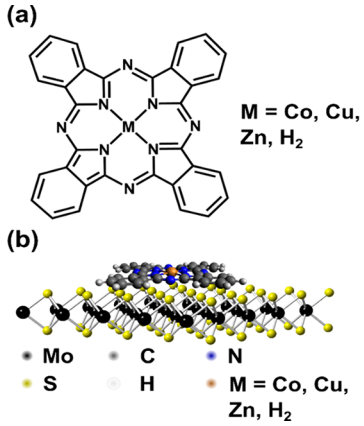


**Figure 1.** (a) Structure of a metallophthalocyanine (MPc) molecule. (b) Schematic of the MPc−$MoS_2$ heterojunction.

for exploring the chemical control of optically active defects in monolayer $MoS_2$. The electronic structures of MPcs can be altered in systematic ways by changing the central metal atom while retaining the aromatic macrocycle framework.[48] In this manner, phthalocyanine−$MoS_2$ mixed-dimensional heterojunctions have been studied to probe PL quenching,[18] Raman enhancement,[20] ultrafast dynamics,[49,50] and interfacial charge transfer and hybridization.[51] In addition, adsorbed titanyl phthalocyanine (TiOPc) has been shown to passivate midgap states in $MoS_2$,[38,39] and adsorbed ZnPc has been shown to suppress the persistent photocurrent in $MoS_2$ photodetectors that originates from trap states[52] as well as to partially quench the defect emission, as discussed above.[40]

It will be shown here that MPcs quench the defect emission of $MoS_2$, with a metal-dependent quenching efficiency that decreases in the order CoPc > CuPc > ZnPc > $H_2$Pc. Gate voltage-dependent PL measurements reveal that this quenching persists to high negative potentials. Furthermore, density functional theory calculations of the defect formation and charge transition energies show that the adsorbed MPcs lower the energy of the negatively charged defects with respect to that of neutral defects through a local electrostatic gating effect, which is in agreement with our experimental observations. The data rule out doping, charge transfer, and nonradiative energy transfer as the primary mechanisms of metallophthalocyanine-based defect PL quenching. Overall, our results provide a molecular-level understanding of adsorbate interactions with luminescent defects in $MoS_2$ and suggest attractive routes for further PL manipulation through molecular adsorbate design.

## EXPERIMENTAL SECTION

**Preparation of Monolayer $MoS_2$.** Monolayer samples of $MoS_2$ were exfoliated via micromechanical exfoliation using Scotch tape on $SiO_2$/Si substrate. To improve the yield of monolayer $MoS_2$, the substrate was heated while in contact with the tape for 15 min at 60 °C and gently exfoliated while still warm. $MoS_2$ monolayers were identified via optical microscopy based on color contrast and then confirmed with Raman microscopy. Identified monolayer samples were then annealed for 4 h at 400 °C in an Ar or $H_2$ environment (constant flow of 600 or 200 sccm, respectively) to remove unwanted tape residues and improve layer adhesion to the $SiO_2$.

**Chemical Vapor Deposition of $MoS_2$ Films.** Monolayer flakes of $MoS_2$ were synthesized using an atmospheric pressure chemical vapor deposition process in which 5 mg of $MoO_3$ (Sigma-Aldrich) powder was spread evenly within an alumina boat and capped with two 1 $cm^2$ $SiO_2$/Si (300 nm oxide) substrates. The alumina boat was


https://doi.org/10.1021/jacs.1c07795
J. Am. Chem. Soc. 2021, 143, 17153−17161

placed inside a 1 in. diameter quartz tube located in the center of a tube furnace. Then, 300 mg of sulfur pieces (Alfa-Aesar) were similarly placed in a second alumina boat that was located upstream and outside of the tube furnace. After purging the sealed quartz tube for 15 min with argon gas, the center of the furnace was heated from room temperature to 700 °C over a span of 40 min. The temperature was then held constant for 3 min. During this entire process, the argon flow rate was maintained at 13 sccm. When the furnace temperature reached 575 °C during the ramp process, the alumina boat containing the sulfur was moved to a region inside the furnace where the temperature was approximately 150 °C as verified by a thermocouple. This movement was enabled by two magnets. Once the growth process was complete, the furnace was allowed to cool to room temperature.

**Metallophthalocyanine Film Deposition.** Cobalt(II) phthalocyanine, zinc(II) phthalocyanine, copper(II) phthalocyanine, and 29*H*,31*H*-phthaloycanine were purchased from Sigma-Aldrich and purified by temperature gradient sublimation by heating one end of a tube furnace containing the crude material under a vacuum of $<10^{-2}$ Torr. Films were grown by thermal evaporation at a pressure below $10^{-5}$ Torr at a rate of 0.1−0.2 Å/s, as monitored by a calibrated quartz crystal microbalance, to obtain a thickness of 1.0 nm.

**Low-Temperature Photoluminescence Measurements.** The photoluminescence (PL) at room temperature (300 K) and at low temperature (10 K) was characterized in a vacuum environment within a variable-temperature optical cryostat (ARS DE204PF) using a 532 nm laser as the excitation source (Lighthouse Photonics, Sprout). The excitation spot was ∼1 $\mu$m using a 100× objective (Nikon T-PLAN with NA 0.6) with an incident power of ∼100 $\mu$W and a 20 s integration time. Emission spectra were collected on a spectrometer (Andor SHAMROCK SR-750 with an i-DUS Camera DU-420A).

**Raman Microscopy.** Confocal Raman microscopy spectra were collected using a Horiba Raman Xplora system with a 532 nm laser, 150 $\mu$W of power, a 100× objective, and 1800 groove/mm diffraction grating.

**TCSPC Microscopy.** Low-temperature time-correlated single photon counting (TCSPC) was carried out in a variable temperature optical cryostat (Montana Instruments Cryostation S100). A 450 nm pulsed laser (Picoquant PDL200b) operating at 500 kHz excited the sample through an objective lens (Zeiss Epiplan-Neofluar 100x/0.90 NA), and the collected fluorescence was directed to an avalanche photodiode detector (APD; Micro Photon Devices PDM) in a confocal arrangement. The fluorescence was separated from the excitation beam via a long pass filter. The timing electronics (Picoquant Picoharp 300) measured the relative time between the arrival of a photon at the APD and a trigger signal from the pulsed laser. The instrument response function (IRF) was obtained by collecting the backscattered light by removing the long pass filter in a spatial region without the sample so that the only the light returning and hitting the APDs was the excitation beam. The IRF of the system is ∼60 ps.

**Density Functional Theory Modeling.** Defect formation energies and projected density of states (pDOS) were obtained from spin-polarized density functional theory (DFT) calculations performed using the Vienna Ab initio Simulation Package (VASP).[53,54] The structural optimization and self-consistent total energy calculations were carried out using the generalized gradient approximation (GGA) and the Perdew−Burke−Ernzerhof (PBE) exchange-correlation functional with DFT-D3 van der Waals corrections[55] along with projector-augmented wave (PAW) potentials.[53] Electronic wave functions were expanded in a plane wave basis set with a kinetic energy cutoff of 400 eV. For the Brillouin zone integration, a 2 × 2 × 1 Monkhorst−Pack *k*-point mesh was used with a *k*-point density of approximately 32 $Å^{-1}$. The energy convergence criterion for the electronic wave function was set to be $10^{-5}$ eV. A vacuum layer of about 13.6 Å (periodic length in the *z*-direction of 20 Å) was chosen to minimize spurious interactions between the periodic layers.

The defect formation energy $E^q_{form}$ at charge state $q$ was calculated by eq 1as follows:[56]

$$E^q_{form} = E^q_{defect} - E_{perfect} - \sum_i n_i\mu_i + qE_{Fermi} + E_{2D\_corr} \quad (1)$$

where $E^q_{defect}$ and $E_{perfect}$ are the total energies of the system with and without defects, respectively, $n_i$ is the number of atoms added or removed by the defect, $\mu_i$ is the chemical potential, and $E_{Fermi}$ is the Fermi level energy. $E_{2D\_corr}$ is the correction term to account for image charge interactions in periodic systems that contain a vacuum gap, and here we apply the scheme developed by Freysoldt and Neugebauer.[57] The defect charge transition level $\varepsilon(q/q')$ is defined as the value of $E_{Fermi}$ for which $E^q_{form} = E^{q'}_{form}$.

For the electronic structure of mixed-dimensional 0D/2D heterojunctions, an electrostatic model that was found to provide results comparable to those of range-separated hybrid functional calculations and experimental band gaps was used and found to be superior over standard DFT calculations.[58] Specifically, we applied self-energy corrections following Neaton et al.[59,60] to both the molecular levels of gas-phase phthalocyanine molecules obtained from the optimally tuned range-separated hybrid functional (OT-RSH)[48] and the band edges of $MoS_2$ to account for the nonlocal dielectric screening effect.[61] Effects of the interface charge redistribution on the energy levels were obtained from DFT calculations with the PBE functional for the 0D/2D heterojunctions. Binding energies of phthalocyanine molecules on $MoS_2$ with a S vacancy and O substitutions were calculated with van der Waals interactions using the Tkatchenko−Scheffler dispersion correction.[62]

## RESULTS AND DISCUSSION

In initial experiments, CoPc was deposited to a thickness of 1.0 nm on mechanically exfoliated monolayer $MoS_2$ as shown in Figure 2a. The monolayer thickness of $MoS_2$ was verified based on the frequency of the $A_{1g}$ and $E^1_{2g}$ phonon modes, which were measured with Raman spectroscopy (Figure 2b), and the CoPc deposition was confirmed by its characteristic Raman modes in the region of 1100−1600 $cm^{-1}$. The Raman modes of CoPc are visible despite the 1 nm film thickness due to known Raman enhancement by the underlying monolayer $MoS_2$.[20,63] Based on prior work on the morphology of MPc−$MoS_2$ films,[20] 1.0 nm of CoPc will result in full CoPc coverage with a range of thicknesses from the monolayer to several-molecule-thick aggregates.

PL spectra were collected before and after CoPc deposition on the same $MoS_2$ flake. At 300 K, the overlapping $MoS_2$ A-exciton and trion emissions are prominent at 670 nm, and a lower wavelength shoulder is assignable to the B-exciton (Figure 2c). Following CoPc deposition, the $MoS_2$ A-exciton is partially quenched (peak area reduced by 59%), which is likely due to mutual charge transfer via the formation of a type II heterojunction.[49] In addition, the PL is shifted to lower wavelengths, which is likely a result of an increased ratio of neutral excitons to trions due to depletion of free $MoS_2$ n-type carriers by the CoPc overlayer. At cryogenic temperatures, the $MoS_2$ defect emission becomes apparent above 700 nm in addition to the previously observed A- and B-excitons (Figure 2d). The A- and B-excitons shift to shorter wavelengths (650 and 600 nm respectively) as expected for $MoS_2$ excitons at a low temperature.[45] Following the deposition of CoPc, the $MoS_2$ A-exciton and trion PL are quenched as in the room temperature PL (area reduced by 53%), while the B-exciton showed minimal change. Most notably, the defect PL is completely quenched at the low temperature following the deposition of CoPc onto $MoS_2$.



https://doi.org/10.1021/jacs.1c07795
J. Am. Chem. Soc. 2021, 143, 17153−17161

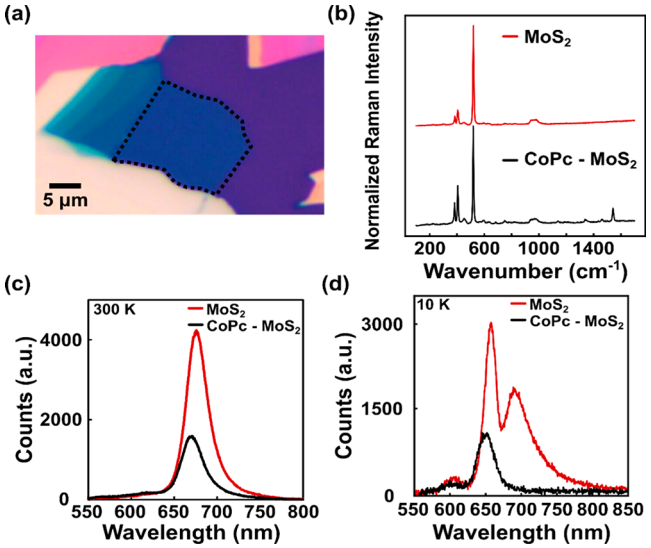


**Figure 2.** (a) Optical micrograph of mechanically exfoliated $MoS_2$ with the monolayer region highlighted. (b) Raman spectra of monolayer $MoS_2$ before and after the deposition of 1 nm CoPc. The separation of the $A_{1g}$ and $E_{2g}$ peaks is ~19 $cm^{-1}$, indicating monolayer $MoS_2$. Raman modes that appear in the 1100−1500 $cm^{-1}$ range are characteristic of CoPc. (c) 300 K PL spectra of mechanically exfoliated $MoS_2$ and $MoS_2$ with 1 nm CoPc. The A-exciton and associated trion are prominent at 675 nm, and a small higher-energy shoulder is visible due to the B-exciton. (d) 10 K PL spectra of $MoS_2$ and $MoS_2$ with 1 nm CoPc. At this temperature, the $MoS_2$ defect emission becomes apparent at 700 nm in addition to the A- and B-excitons at 660 and 600 nm, respectively. The defect PL is completely quenched by the CoPc film, and the A-exciton is partially quenched.

To investigate the mechanism of the observed defect PL quenching, the variation in defect PL was compared for a range of MPc derivatives (M = Co, Cu, Zn, and $H_2$). For a direct comparison between different molecules, chemical vapor deposition (CVD) was used to synthesize $MoS_2$, yielding a higher concentration of defects such as sulfur vacancies.[64] This deposition method results in defect PL that is an order of magnitude more intense than the A-exciton and thus accentuates the differences in the quenching behavior between the various MPcs. To avoid spatial inhomogeneity, 1.0 nm MPc films were deposited in different regions of a large-area $MoS_2$ monolayer film via shadow masking (Figure 3a). Since the crystalline quality and stoichiometry of CVD-derived $MoS_2$ can vary along the growth direction, this masking approach allows the defect PL to be compared between pristine $MoS_2$ and the nearby MPc−$MoS_2$ heterojunction that nominally has the same growth quality.

Figure 3b compares the defect PL quenching efficiency of the different MPc structures. As expected from higher defect density in CVD $MoS_2$, the defect emission is more intense than the excitonic emission in these samples compared with those of the mechanically exfoliated samples in Figure 2d. A clear trend in intensity for the defect PL peak is observed among the different MPcs, with CoPc being the strongest quencher, followed by CuPc, ZnPc, and finally $H_2$Pc with the lowest quenching efficiency. Figure 3c plots the quenching fraction (QF), which is defined by eq 2 as follows:

$$\mathrm{QF} = 1 - \frac{\sum_{675}^{900} \mathrm{PL(MPc - MoS_2)}}{\sum_{675}^{900} \mathrm{PL(MoS_2)}} \quad (2)$$

PL(MPc−$MoS_2$) is the non-normalized PL spectrum of the MPc−$MoS_2$ heterojunction, PL($MoS_2$) is the non-normalized PL of the nearby bare $MoS_2$, and the $\sum$ operator denotes a Riemann sum of the curves over the indicated wavelengths. A quenching fraction of 1.0 means the complete disappearance of the defect PL peak, and a quenching fraction of 0 indicates no change in the defect PL. Thus, the peak areas follow the same trend as the peak height shown in Figure 3b, with the quenching fraction following the order $QF_{CoPc} > QF_{CuPc} > QF_{ZnPc} > QF_{H_2Pc}$.

To verify the assigned PL quenching behavior, time-resolved PL measurements were carried out at low temperatures (10 K) using time-correlated single photon counting (TCSPC). Figure 4 shows the decay of the PL from defects in $MoS_2$ and the $MoS_2$−MPc heterojunctions. The defect PL in pristine $MoS_2$ is known to have a lifetime of several microseconds, far longer than the exciton lifetime of ~100 ps.[29] The excitonic and defect PL were not spectrally resolved in this experiment but could be differentiated based on the large expected difference in their lifetimes. Due to instrumental limitations, we are only able to collect TCSPC traces out to 2 μs, which does not allow an accurate fitting of the long defect PL decay times. Nevertheless, a qualitative estimation of the defect-associated exciton decay rates can be obtained by linearly fitting the log-plots to the trace for times greater than 100 ns since the A-exciton emission has a significantly shorter lifetime (600 ps at 300 K and 150 ps at 77 K)[29] and is not expected to contribute

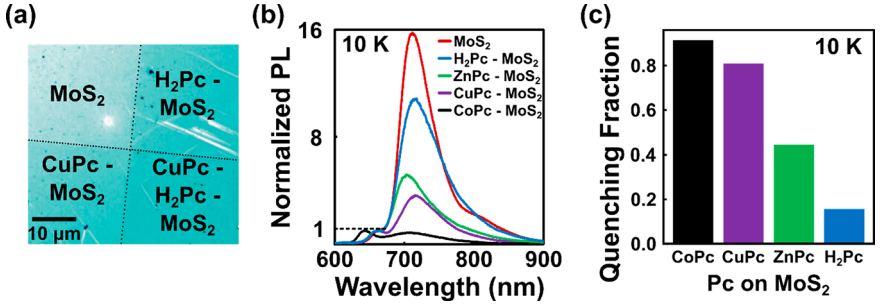


**Figure 3.** (a) Optical microscopy images of representative MPc films on monolayer CVD $MoS_2$. $MoS_2$ PL spectra were collected near the edges of the MPc film to ensure that the observed quenching was not due to inhomogeneity in the CVD growth. (b) Low-temperature photoluminescence spectra of representative CVD $MoS_2$ and $MoS_2$ with 1 nm films of $H_2$Pc, ZnPc, CuPc, and CoPc. The spectra are normalized to the intensities of their respective $MoS_2$ A-exciton peaks. The non-normalized PL plots and reference $MoS_2$ spectra are shown in Figure S1. (c) Comparison of the $MoS_2$ defect PL quenching fraction for each MPc.



https://doi.org/10.1021/jacs.1c07795
J. Am. Chem. Soc. 2021, 143, 17153−17161

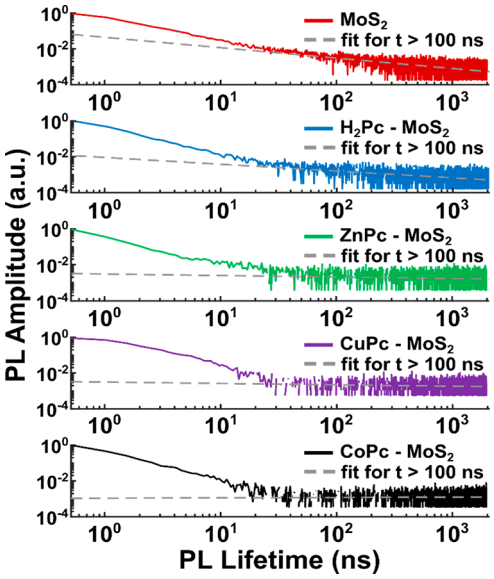


**Figure 4.** Time-correlated single photon counting (TCSPC) traces collected at 10 K with a 450 nm laser showing the photoluminescence decay for $MoS_2$ and the indicated $MoS_2$−MPc systems. Due to instrumentation limitations, the defect emission microsecond-scale decay cannot be accurately fit but can allow qualitative comparisons using a linear fit to the median intensity for times >100 ns.

at these longer times. The relative slopes in the log-plots of these lines are then the relative magnitudes of the defect PL decay. The pristine $MoS_2$ shows the expected microsecond-scale decay of the defect signal (estimated to be 4 $\mu$s at 77 K),[29] while $MoS_2$−$H_2Pc$ exhibits a smaller slope and ZnPc, CuPc, and CoPc are qualitatively similar, revealing no single-microsecond decay dynamics associated with defect-bound $MoS_2$ excitons. The absence of PL decay associated with the radiative recombination of defect excitons in MPc−$MoS_2$ indicates that the MPcs are either creating a new nonradiative decay pathway that outcompetes the radiative decay from defect-bound excitons or eliminating the defect-bound exciton radiative decay pathway altogether. Both these processes would result in the observed decrease in the amplitude of the defect PL.

The mechanisms for quenching the defect PL include creating faster competing recombination pathways through energy or charge transfer and the elimination of the defect−exciton recombination pathway altogether through either modifying the Fermi level or altering the chemistry of the defect itself. Let us first consider nonradiative energy transfer (NRET) in which the defect excited state transfers energy to the MPc, where it decays without emitting a photon. For systems in the weak electronic coupling regime, the rate of the energy transfer is proportional to the spectral overlap of the donor PL spectrum and the acceptor absorbance spectrum.[65] The computed overlap integrals for CoPc, CuPc, ZnPc, and $H_2Pc$ are shown in Figure S2, and the corresponding data are compiled in Table S1. These indicate that the observed quenching fraction has no correlation with the spectral overlap, implying that NRET is not the primary mechanism of defect PL quenching. The damping of the $MoS_2$ dielectric function by the MPcs is a similar PL quenching mechanism,[66,67] but this also does not reproduce the observed trend in the quenching fraction QF(Co > Cu > Zn > $H_2$), instead predicting more quenching of the defect PL by $H_2Pc$ than that by CuPc (Figure S3). More information about this mechanism can be found in the SI.

The mechanism of the metallophthalocyanine-based defect PL quenching was further investigated by studying the gate voltage dependence of the defect emission at a low temperature (10 K), allowing the Fermi level to be tuned to quench thermionic processes. Bare $MoS_2$ devices (Figure 5a)

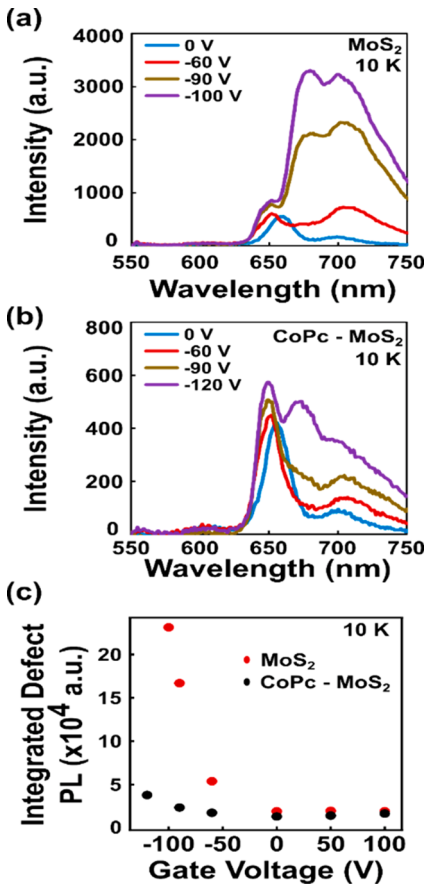


**Figure 5.** Low-temperature PL spectra with applied gate voltages for (a) mechanically exfoliated $MoS_2$ alone and (b) CoPc−$MoS_2$. Negative gate voltages enhance the defect emission in $MoS_2$, but this effect is suppressed by CoPc. (c) Comparison of the integrated defect PL for $MoS_2$ and CoPc−$MoS_2$ at the indicated gate voltages.

show the expected Fermi level dependence, with the defect emission dramatically increasing with the decreasing gate voltage in agreement with the literature.[32] In contrast, CoPc−$MoS_2$ devices (Figure 5b) suppress the defect emission out to large negative gate voltages, only exhibiting substantial defect emissions below −100 V. These results are summarized in Figure 5c.

Note that at positive gate voltages both $MoS_2$ and CoPc−$MoS_2$ show little change in their defect PL emission (Figure S4); however, CoPc−$MoS_2$ exhibits a greater shift in the excitonic emission to a lower energy. This observation is consistent with CoPc−$MoS_2$ having a larger population of neutral excitons at 0 V, as observed in Figures 3 and S6, which shifts to trion-dominated emission at 100 V. $MoS_2$ alone is trion-dominated at both 0 and 100 V, causing a greater apparent shift for $MoS_2$−CoPc. This effect is explained by $MoS_2$ being naturally electron-doped and able to accommodate a greater fraction of trions at the zero gate voltage versus


https://doi.org/10.1021/jacs.1c07795
J. Am. Chem. Soc. 2021, 143, 17153−17161

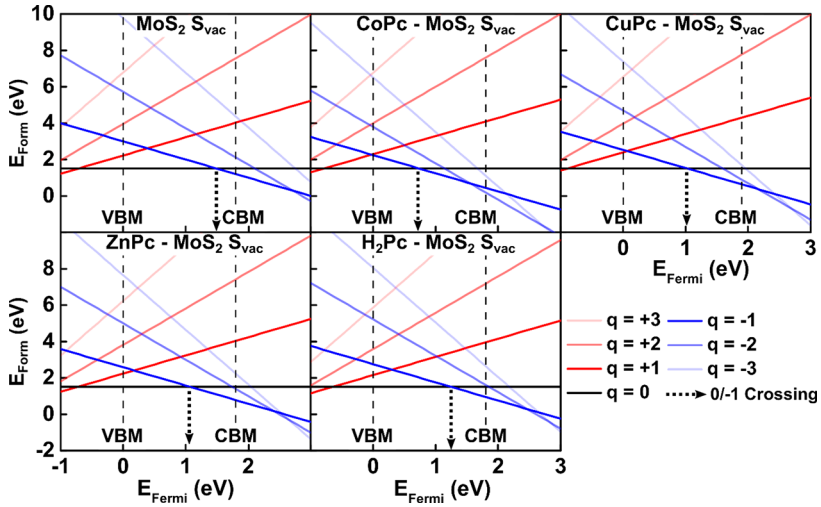


**Figure 6.** The formation energy of neutral and charged $S_{vac}$ versus the Fermi energy for $MoS_2$ alone, CoPc−$MoS_2$, CuPc−$MoS_2$, ZnPc−$MoS_2$, and $H_2$Pc−$MoS_2$. For a given Fermi energy, the dominant defect state is the charged state corresponding to the lowest energy line. In the case of $MoS_2$ without Pc, $S_{vac}$ is neutral when the Fermi energy equals the VBM and has a charge of −1 when the Fermi energy equals the CBM. At Fermi levels near the CBM, the order of the formation energy of the negative $S_{vac}$ is CoPc < CuPc < ZnPc < $H_2$Pc < $MoS_2$ only. The Fermi energy where the defect charge changes from neutral to negative ($\varepsilon(0/-1)$) is highlighted with a gray arrow.

the depleted $MoS_2$−CoPc p−n heterojunction diode. From this perspective, one should expect more defect PL following CoPc adsorption since charge depletion or doping should have the same effect as a negative gate bias as in Figure 5a. Comparing the $MoS_2$ excitonic PL energy before and after MPc deposition (Figure S5), we see that all the investigated MPcs form depleted heterojunctions to varying degrees, which is in agreement with literature electrical measurements showing increased threshold voltages in MPc−$MoS_2$ field-effect transistors.[18,52,68] Since molecule-induced doping should increase defect emission in the case of MPc, contrary to our observations, it can be ruled out as the primary mechanism of quenching.

To further narrow the possible mechanisms of the observed defect PL quenching, a detailed DFT analysis was applied. First, the interaction between MPc molecules and $MoS_2$ point defects was verified to be energetically favorable. Figure S6 shows that MPcs bind near both sulfur vacancies ($S_{vac}$) and oxygen substitutions ($O_{sub}$), with the outer carbon aromatic ring directly above the defect being the most energetically favorable position. As noted above, another potential mechanism of defect quenching is excited-state charge transfer from the $MoS_2$ defect states to the molecule. While thermally activated electron transfer processes are typically vibration-coupled and thus require more thermal energy than is available at 10 K ($k_BT \approx 7$ cm$^{-1}$), charge transfer can still occur via tunneling.[69] Tunneling-assisted charge transfer strongly depends on the energy level alignment in the heterostructure, which in turn depends on the metal center of the MPc.[20,48] Our computed projected density of states (pDOS) of localized defect states (Figure S7a) and orbital energy levels for the MPc and $H_2$Pc on $MoS_2$ (Figure S7b) show the energy of the nonfrontier out-of-plane d-orbital decreasing with increasing atomic number of the metal center. The CoPc HOMO − 1 is near-resonant with the valence band maximum of $MoS_2$, suggesting a possible coupling with defect states near the valence band. Nevertheless, as shown in the SI, the expected variation of tunneling currents, which is proportional to the near-constant density of states in the valence band, does not match the observed trends in the quenching efficiency, thus ruling out tunneling as a primary source of defect quenching.

In contrast, the charge transition levels of defects show significant variation upon MPc adsorption. Figure 6 shows the computed formation energy of different charged states as a function of the Fermi energy for the sulfur vacancies of $MoS_2$ alone and the MPc−$MoS_2$ heterojunctions. A similar calculation was also performed for oxygen substitutional impurities as shown in Figure S8. Specifically, MPc adsorption introduces a decrease in the Fermi energy at which the defect charge state changes from 0 to −1, a change that is in agreement with the experimental trend. At higher gate voltages, the Fermi level is near the CBM, the defect PL is weak, and the defects are negatively charged. As the gate voltage decreases, the defect PL increases as the defect charge changes from negative to neutral. In the case of MPc−$MoS_2$, there is a trend in the Fermi level where the favored defect changes from neutral ($q = 0$) to negative ($q = -1$) that follows the observed trend in the quenching factor, with the negative defect stabilized the most by CoPc, followed by CuPc, ZnPc, and finally $H_2$Pc. For Pc−$MoS_2$, the population of negative (dark) defects is greater and a far lower gate voltage is required to drive the defects to neutral (bright), which is in agreement with the observations in Figure 5b. Having ruled out other potential PL quenching mechanisms, our results argue that the MPcs quench defect PL by altering the charge of the defects themselves rather than creating competing nonradiative decay paths.

These data suggest a trend in the chemistry of the MPcs that results in changes in their interactions with $MoS_2$ defects. One source of this trend is the electrostatic potential of the outer carbon rings of the MPc that sits above the $MoS_2$ $S_{vac}$ (Figure S9). Due to changes in the polarization of the metal−Pc bonding, the potential of this carbon ring above the $S_{vac}$ follows the trend CoPc > CuPc > ZnPc > $H_2$Pc, as summarized in Table S2. The positive electrostatic potential above the $S_{vac}$ will stabilize a negative charge, which is consistent with the observed trend in our data and suggests design rules for altering the chemistry of defects with other molecules.



https://doi.org/10.1021/jacs.1c07795
J. Am. Chem. Soc. 2021, 143, 17153−17161

## CONCLUSIONS

We have demonstrated the quenching of the $MoS_2$ defect photoluminescence by the deposition of MPc thin films, where the quenching efficiency depends sensitively on the central transition metal. Experiments rule out nonradiative energy transfer, charge depletion, and charge transfer as the mechanisms of this quenching. Gate voltage-dependent measurements and DFT analysis suggest that the mechanism of PL quenching is the stabilization of negatively charged defects by MPc. The different quenching behaviors of the various MPcs suggest a powerful route to controlling defect chemistry through molecular adsorbates. This result has significant implications for improving $MoS_2$-based single photon emitters by quenching the background defect PL and may also be used to manipulate populations of defect-bound excitons to increase the PLQY at high excitation powers.

## ASSOCIATED CONTENT

### Supporting Information

The Supporting Information is available free of charge at https://pubs.acs.org/doi/10.1021/jacs.1c07795.

Non-normalized PL spectra, nonradiative energy transfer models, PL spectra at positive gate voltages, normalized room temperature PL, Pc binding energy calculations on $MoS_2$ defects, pDOS and orbital energies, formation energy of oxygen substitutions, and phthalocyanines electrostatics (PDF)

## AUTHOR INFORMATION


### Corresponding Authors

**Pierre Darancet** − *Center for Nanoscale Materials, Argonne National Laboratory, Lemont, Illinois 60439, United States; Northwestern Argonne Institute of Science and Engineering, Evanston, Illinois 60208, United States*; Email: pdarancet@anl.com

**Maria K. Y. Chan** − *Center for Nanoscale Materials, Argonne National Laboratory, Lemont, Illinois 60439, United States; Northwestern Argonne Institute of Science and Engineering, Evanston, Illinois 60208, United States*; Email: mchan@anl.gov

**Mark C. Hersam** − *Department of Chemistry and the Materials Research Center, Department of Materials Science and Engineering and the Materials Research Center, and Department of Electrical and Computer Engineering and the Materials Research Center, Northwestern University, Evanston, Illinois 60208, United States;* orcid.org/0000-0003-4120-1426; Email: m-hersam@northwestern.edu

**Nathaniel P. Stern** − *Department of Physics and Astronomy, Northwestern University, Evanston, Illinois 60208, United States;* orcid.org/0000-0002-8903-3516; Email: n-stern@northwestern.edu

**Tobin J. Marks** − *Department of Chemistry and the Materials Research Center and Department of Materials Science and Engineering and the Materials Research Center, Northwestern University, Evanston, Illinois 60208, United States;* orcid.org/0000-0001-8771-0141; Email: t-marks@northwestern.edu

### Authors

**Samuel H. Amsterdam** − *Department of Chemistry and the Materials Research Center, Northwestern University, Evanston, Illinois 60208, United States*

**Teodor K. Stanev** − *Department of Physics and Astronomy, Northwestern University, Evanston, Illinois 60208, United States*

**Luqing Wang** − *Center for Nanoscale Materials, Argonne National Laboratory, Lemont, Illinois 60439, United States; Department of Materials Science and Engineering and the Materials Research Center, Northwestern University, Evanston, Illinois 60208, United States*

**Qunfei Zhou** − *Center for Nanoscale Materials, Argonne National Laboratory, Lemont, Illinois 60439, United States; Department of Materials Science and Engineering and the Materials Research Center, Northwestern University, Evanston, Illinois 60208, United States;* orcid.org/0000-0002-8499-1993

**Shawn Irgen-Gioro** − *Department of Chemistry and the Materials Research Center, Northwestern University, Evanston, Illinois 60208, United States*

**Suyog Padgaonkar** − *Department of Chemistry and the Materials Research Center, Northwestern University, Evanston, Illinois 60208, United States*

**Akshay A. Murthy** − *Department of Materials Science and Engineering and the Materials Research Center, Northwestern University, Evanston, Illinois 60208, United States;* orcid.org/0000-0001-7677-6866

**Vinod K. Sangwan** − *Department of Materials Science and Engineering and the Materials Research Center, Northwestern University, Evanston, Illinois 60208, United States;* orcid.org/0000-0002-5623-5285

**Vinayak P. Dravid** − *Department of Materials Science and Engineering and the Materials Research Center, Northwestern University, Evanston, Illinois 60208, United States; Northwestern University Atomic and Nanoscale Characterization Experimental (NUANCE) Center, Evanston, Illinois 60208, United States;* orcid.org/0000-0002-6007-3063

**Emily A. Weiss** − *Department of Chemistry and the Materials Research Center, Department of Physics and Astronomy, and Department of Materials Science and Engineering and the Materials Research Center, Northwestern University, Evanston, Illinois 60208, United States;* orcid.org/0000-0001-5834-463X

Complete contact information is available at: https://pubs.acs.org/10.1021/jacs.1c07795


### Notes

The authors declare no competing financial interest.

## ACKNOWLEDGMENTS

This work was primarily supported by the National Science Foundation Materials Research Science and Engineering Center at Northwestern University (DMR-1720319). CVD growth of $MoS_2$ by V.P.D. and A.A.M. was also supported by the National Science Foundation under Grant No. DMR-1929356. A.A.M. gratefully acknowledges support from the Ryan Fellowship and the IIN at Northwestern University. Use of the Center for Nanoscale Materials (CNM), an Office of Science user facility, was supported by the U.S. Department of Energy, Office of Science, Office of Basic Energy Sciences, under Contract DE-AC02-06CH11357. We gratefully acknowledge use of the Bebop cluster in the Laboratory Computing Resource Center at Argonne National Laboratory. This research was supported in part through the computational

resources and staff contributions provided for the Quest high performance computing facility at Northwestern University, which is jointly supported by the Office of the Provost, the Office for Research, and Northwestern University Information Technology.

## REFERENCES

(1) Jariwala, D.; Sangwan, V. K.; Lauhon, L. J.; Marks, T. J.; Hersam, M. C. Emerging Device Applications for Semiconducting Two-Dimensional Transition Metal Dichalcogenides. *ACS Nano* **2014**, *8*, 1102−1120.
(2) Singh, E.; Singh, P.; Kim, K. S.; Yeom, G. Y.; Nalwa, H. S. Flexible Molybdenum Disulfide ($MoS_2$) Atomic Layers for Wearable Electronics and Optoelectronics. *ACS Appl. Mater. Interfaces* **2019**, *11*, 11061−11105.
(3) Barua, S.; Dutta, H. S.; Gogoi, S.; Devi, R.; Khan, R. Nanostructured $MoS_2$-Based Advanced Biosensors: A Review. *ACS Appl. Nano Mater.* **2018**, *1*, 2−25.
(4) Sui, X.; Downing, J. R.; Hersam, M. C.; Chen, J. Additive Manufacturing and Applications of Nanomaterial-Based Sensors. *Mater. Today* **2021**, DOI: 10.1016/j.mattod.2021.02.001.
(5) Wang, L.; Huang, L.; Tan, W. C.; Feng, X.; Chen, L.; Huang, X.; Ang, K.-W. 2D Photovoltaic Devices: Progress and Prospects. *Small Methods* **2018**, *2*, 1700294.
(6) Brar, V. W.; Sherrott, M. C.; Jariwala, D. Emerging Photonic Architectures in Two-Dimensional Opto-Electronics. *Chem. Soc. Rev.* **2018**, *47*, 6824−6844.
(7) Lee, H. S.; Sangwan, V. K.; Rojas, W. A. G.; Bergeron, H.; Jeong, H. Y.; Yuan, J.; Su, K.; Hersam, M. C. Dual-Gated $MoS_2$ Memtransistor Crossbar Array. *Adv. Funct. Mater.* **2020**, *30*, 2003683.
(8) Sangwan, V. K.; Hersam, M. C. Neuromorphic Nanoelectronic Materials. *Nat. Nanotechnol.* **2020**, *15*, 517−528.
(9) Sangwan, V. K.; Lee, H. S.; Bergeron, H.; Balla, I.; Beck, M. E.; Chen, K. S.; Hersam, M. C. Multi-Terminal Memtransistors from Polycrystalline Monolayer Molybdenum Disulfide. *Nature* **2018**, *554*, 500−504.
(10) Ding, Q.; Song, B.; Xu, P.; Jin, S. Efficient Electrocatalytic and Photoelectrochemical Hydrogen Generation Using $MoS_2$ and Related Compounds. *Chem.* **2016**, *1*, 699−726.
(11) Wang, H.; Li, C.; Fang, P.; Zhang, Z.; Zhang, J. Z. Synthesis, Properties, and Optoelectronic Applications of Two-Dimensional $MoS_2$ and $MoS_2$-Based Heterostructures. *Chem. Soc. Rev.* **2018**, *47*, 6101−6127.
(12) Padgaonkar, S.; Olding, J. N.; Lauhon, L. J.; Hersam, M. C.; Weiss, E. A. Emergent Optoelectronic Properties of Mixed-Dimensional Heterojunctions. *Acc. Chem. Res.* **2020**, *53*, 763−772.
(13) Amsterdam, S. H.; Marks, T. J.; Hersam, M. C. Leveraging Molecular Properties to Tailor Mixed-Dimensional Heterostructures beyond Energy Level Alignment. *J. Phys. Chem. Lett.* **2021**, *12*, 4543−4557.
(14) Gobbi, M.; Orgiu, E.; Samorì, P. When 2D Materials Meet Molecules: Opportunities and Challenges of Hybrid Organic/Inorganic van Der Waals Heterostructures. *Adv. Mater.* **2018**, *30*, 1706103.
(15) Huang, Y. L.; Zheng, Y. J.; Song, Z.; Chi, D.; Wee, A. T. S.; Quek, S. Y. The Organic-2D Transition Metal Dichalcogenide Heterointerface. *Chem. Soc. Rev.* **2018**, *47*, 3241−3264.
(16) Sun, J.; Choi, Y.; Choi, Y. J.; Kim, S.; Park, J.; Lee, S.; Cho, J. H. 2D−Organic Hybrid Heterostructures for Optoelectronic Applications. *Adv. Mater.* **2019**, *31*, 1803831.
(17) Shastry, T. A.; Balla, I.; Bergeron, H.; Amsterdam, S. H.; Marks, T. J.; Hersam, M. C. Mutual Photoluminescence Quenching and Photovoltaic Effect in Large-Area Single-Layer $MoS_2$ − Polymer Heterojunctions. *ACS Nano* **2016**, *10*, 10573−10579.
(18) Choi, J.; Zhang, H.; Choi, J. H. Modulating Optoelectronic Properties of Two-Dimensional Transition Metal Dichalcogenide Semiconductors by Photoinduced Charge Transfer. *ACS Nano* **2016**, *10*, 1671−1680.
(19) Zhang, L.; Sharma, A.; Zhu, Y.; Zhang, Y.; Wang, B.; Dong, M.; Nguyen, H. T.; Wang, Z.; Wen, B.; Cao, Y.; et al. Efficient and Layer-Dependent Exciton Pumping across Atomically Thin Organic−Inorganic Type-I Heterostructures. *Adv. Mater.* **2018**, *30*, 1803986.
(20) Amsterdam, S. H.; Stanev, T. K.; Zhou, Q.; Lou, A. J.-T.; Bergeron, H.; Darancet, P.; Hersam, M. C.; Stern, N. P.; Marks, T. J. Electronic Coupling in Metallophthalocyanine−Transition Metal Dichalcogenide Mixed-Dimensional Heterojunctions. *ACS Nano* **2019**, *13*, 4183−4190.
(21) Amani, M.; Taheri, P.; Addou, R.; Ahn, G. H.; Kiriya, D.; Lien, D. H.; Ager, J. W.; Wallace, R. M.; Javey, A. Recombination Kinetics and Effects of Superacid Treatment in Sulfur- and Selenium-Based Transition Metal Dichalcogenides. *Nano Lett.* **2016**, *16*, 2786−2791.
(22) Zhou, M.; Wang, W.; Lu, J.; Ni, Z. How Defects Influence the Photoluminescence of TMDCs. *Nano Res.* **2021**, *14*, 29−39.
(23) Cho, K.; Pak, J.; Chung, S.; Lee, T. Recent Advances in Interface Engineering of Transition-Metal Dichalcogenides with Organic Molecules and Polymers. *ACS Nano* **2019**, *13*, 9713−9734.
(24) Liu, X.; Hersam, M. C. 2D Materials for Quantum Information Science. *Nat. Rev. Mater.* **2019**, *4*, 669−684.
(25) Qiu, H.; Xu, T.; Wang, Z.; Ren, W.; Nan, H.; Ni, Z.; Chen, Q.; Yuan, S.; Miao, F.; Song, F.; et al. Hopping Transport through Defect-Induced Localized States in Molybdenum Disulphide. *Nat. Commun.* **2013**, *4*, 1−6.
(26) Murthy, A. A.; Stanev, T. K.; Dos Reis, R.; Hao, S.; Wolverton, C.; Stern, N. P.; Dravid, V. P. Direct Visualization of Electric-Field-Induced Structural Dynamics in Monolayer Transition Metal Dichalcogenides. *ACS Nano* **2020**, *14*, 1569−1576.
(27) Huang, B.; Tian, F.; Shen, Y.; Zheng, M.; Zhao, Y.; Wu, J.; Liu, Y.; Pennycook, S. J.; Thong, J. T. L. Selective Engineering of Chalcogen Defects in $MoS_2$ by Low-Energy Helium Plasma. *ACS Appl. Mater. Interfaces* **2019**, *11*, 24404−24411.
(28) Liu, X.; Balla, I.; Bergeron, H.; Hersam, M. C. Point Defects and Grain Boundaries in Rotationally Commensurate $MoS_2$ on Epitaxial Graphene. *J. Phys. Chem. C* **2016**, *120*, 20798−20805.
(29) Goodman, A. J.; Willard, A. P.; Tisdale, W. A. Exciton Trapping Is Responsible for the Long Apparent Lifetime in Acid-Treated $MoS_2$. *Phys. Rev. B: Condens. Matter Mater. Phys.* **2017**, *96*, 121404.
(30) Verhagen, T.; Guerra, V. L. P.; Haider, G.; Kalbac, M.; Vejpravova, J. Towards the Evaluation of Defects in $MoS_2$ Using Cryogenic Photoluminescence Spectroscopy. *Nanoscale* **2020**, *12*, 3019.
(31) Saigal, N.; Ghosh, S. Evidence for Two Distinct Defect Related Luminescence Features in Monolayer $MoS_2$. *Appl. Phys. Lett.* **2016**, *109*, 122105.
(32) Greben, K.; Arora, S.; Harats, M. G.; Bolotin, K. I. Intrinsic and Extrinsic Defect-Related Excitons in TMDCs. *Nano Lett.* **2020**, *20*, 2544−2550.
(33) Barthelmi, K.; Klein, J.; Hötger, A.; Sigl, L.; Sigger, F.; Mitterreiter, E.; Rey, S.; Gyger, S.; Lorke, M.; Florian, M.; et al. Atomistic Defects as Single-Photon Emitters in Atomically Thin $MoS_2$. *Appl. Phys. Lett.* **2020**, *117*, 070501.
(34) Klein, J.; Lorke, M.; Florian, M.; Sigger, F.; Sigl, L.; Rey, S.; Wierzbowski, J.; Cerne, J.; Müller, K.; Mitterreiter, E.; et al. Site-Selectively Generated Photon Emitters in Monolayer $MoS_2$ via Local Helium Ion Irradiation. *Nat. Commun.* **2019**, *10*, 1−8.
(35) Goodman, A. J.; Lien, D. H.; Ahn, G. H.; Spiegel, L. L.; Amani, M.; Willard, A. P.; Javey, A.; Tisdale, W. A. Substrate-Dependent Exciton Diffusion and Annihilation in Chemically Treated $MoS_2$ and $WS_2$. *J. Phys. Chem. C* **2020**, *124*, 12175−12184.
(36) Cadiz, F.; Courtade, E.; Robert, C.; Wang, G.; Shen, Y.; Cai, H.; Taniguchi, T.; Watanabe, K.; Carrere, H.; Lagarde, D.; et al. Excitonic Linewidth Approaching the Homogeneous Limit in MoS2-Based van Der Waals Heterostructures. *Phys. Rev. X* **2017**, *7*, 021026.
(37) Lu, H.; Kummel, A.; Robertson, J. Passivating the Sulfur Vacancy in Monolayer $MoS_2$. *APL Mater.* **2018**, *6*, 066104.
(38) Park, J. H.; Sanne, A.; Guo, Y.; Amani, M.; Zhang, K.; Movva, H. C. P. P.; Robinson, J. A.; Javey, A.; Robertson, J.; Banerjee, S. K.;

et al. Defect Passivation of Transition Metal Dichalcogenides via a Charge Transfer van Der Waals Interface. *Sci. Adv.* **2017**, *3*, e1701661.
(39) Choudhury, P.; Ravavarapu, L.; Dekle, R.; Chowdhury, S. Modulating Electronic and Optical Properties of Monolayer $MoS_2$ Using Nonbonded Phthalocyanine Molecules. *J. Phys. Chem. C* **2017**, *121*, 2959−2967.
(40) Ahn, H.; Huang, Y. C.; Lin, C. W.; Chiu, Y. L.; Lin, E. C.; Lai, Y. Y.; Lee, Y. H. Efficient Defect Healing of Transition Metal Dichalcogenides by Metallophthalocyanine. *ACS Appl. Mater. Interfaces* **2018**, *10*, 29145−29152.
(41) Haldar, S.; Vovusha, H.; Yadav, M. K.; Eriksson, O.; Sanyal, B. Systematic Study of Structural, Electronic, and Optical Properties of Atomic-Scale Defects in the Two-Dimensional Transition Metal Dichalcogenides $MX_2$ (M = Mo, W; X = S, Se, Te). *Phys. Rev. B: Condens. Matter Mater. Phys.* **2015**, *92*, 235408.
(42) Zhou, W.; Zou, X.; Najmaei, S.; Liu, Z.; Shi, Y.; Kong, J.; Lou, J.; Ajayan, P. M.; Yakobson, B. I.; Idrobo, J.-C. Intrinsic Structural Defects in Monolayer Molybdenum Disulfide. *Nano Lett.* **2013**, *13*, 2615−2622.
(43) Barja, S.; Refaely-Abramson, S.; Schuler, B.; Qiu, D. Y.; Pulkin, A.; Wickenburg, S.; Ryu, H.; Ugeda, M. M.; Kastl, C.; Chen, C.; et al. Identifying Substitutional Oxygen as a Prolific Point Defect in Monolayer Transition Metal Dichalcogenides. *Nat. Commun.* **2019**, *10*, 1−8.
(44) Pető, J.; Ollár, T.; Vancsó, P.; Popov, Z. I.; Magda, G. Z.; Dobrik, G.; Hwang, C.; Sorokin, P. B.; Tapasztó, L. Spontaneous Doping of the Basal Plane of $MoS_2$ Single Layers through Oxygen Substitution under Ambient Conditions. *Nat. Chem.* **2018**, *10*, 1246−1251.
(45) Tongay, S.; Suh, J.; Ataca, C.; Fan, W.; Luce, A.; Kang, J. S.; Liu, J.; Ko, C.; Raghunathanan, R.; Zhou, J.; et al. Defects Activated Photoluminescence in Two-Dimensional Semiconductors: Interplay between Bound, Charged, and Free Excitons. *Sci. Rep.* **2013**, *3*, 1−5.
(46) Sivaram, S. V.; Hanbicki, A. T.; Rosenberger, M. R.; Jernigan, G. G.; Chuang, H. J.; McCreary, K. M.; Jonker, B. T. Spatially Selective Enhancement of Photoluminescence in $MoS_2$ by Exciton-Mediated Adsorption and Defect Passivation. *ACS Appl. Mater. Interfaces* **2019**, *11*, 16147−16155.
(47) Voronina, E. N.; Mankelevich, Y. A.; Novikov, L. S.; Rakhimova, T. V.; Marinov, D.; de Marneffe, J.-F. Mechanisms of Hydrogen Atom Interactions with $MoS_2$ Monolayer. *J. Phys.: Condens. Matter* **2020**, *32*, 445003.
(48) Zhou, Q.; Liu, Z.-F.; Marks, T. J.; Darancet, P. Electronic Structure of Metallophthalocyanines, MPc (M = Fe, Co, Ni, Cu, Zn, Mg) and Fluorinated MPc. *J. Phys. Chem. A* **2021**, *125*, 4055−4061.
(49) Padgaonkar, S.; Amsterdam, S. H.; Bergeron, H.; Su, K.; Marks, T. J.; Hersam, M. C.; Weiss, E. A. Molecular-Orientation-Dependent Interfacial Charge Transfer in Phthalocyanine/$MoS_2$ Mixed-Dimensional Heterojunctions. *J. Phys. Chem. C* **2019**, *123*, 13337−13343.
(50) Kafle, T. R.; Kattel, B.; Yao, P.; Zereshki, P.; Zhao, H.; Chan, W.-L. Effect of the Interfacial Energy Landscape on Photoinduced Charge Generation at the ZnPc/$MoS_2$ Interface. *J. Am. Chem. Soc.* **2019**, *141*, 11328−11336.
(51) Greulich, K.; Belser, A.; Bölke, S.; Grüninger, P.; Karstens, R.; Sättele, M. S.; Ovsyannikov, R.; Giangrisostomi, E.; Basova, T. V.; Klyamer, D.; et al. Charge Transfer from Organic Molecules to Molybdenum Disulfide: Influence of the Fluorination of Iron Phthalocyanine. *J. Phys. Chem. C* **2020**, *124*, 16990−16999.
(52) Huang, Y.; Zhuge, F.; Hou, J.; Lv, L.; Luo, P.; Zhou, N.; Gan, L.; Zhai, T. Van Der Waals Coupled Organic Molecules with Monolayer $MoS_2$ for Fast Response Photodetectors with Gate-Tunable Responsivity. *ACS Nano* **2018**, *12*, 4062−4073.
(53) Kresse, G.; Joubert, D. From Ultrasoft Pseudopotentials to the Projector Augmented-Wave Method. *Phys. Rev. B: Condens. Matter Mater. Phys.* **1999**, *59*, 1758−1775.
(54) Kresse, G.; Furthmüller, J. Efficient Iterative Schemes for Ab Initio Total-Energy Calculations Using a Plane-Wave Basis Set. *Phys. Rev. B: Condens. Matter Mater. Phys.* **1996**, *54*, 11169−11186.
(55) Grimme, S.; Antony, J.; Ehrlich, S.; Krieg, H. A Consistent and Accurate *Ab Initio* Parametrization of Density Functional Dispersion Correction (DFT-D) for the 94 Elements H-Pu. *J. Chem. Phys.* **2010**, *132*, 154104.
(56) Freysoldt, C.; Grabowski, B.; Hickel, T.; Neugebauer, J.; Kresse, G.; Janotti, A.; Van De Walle, C. G. First-Principles Calculations for Point Defects in Solids. *Rev. Mod. Phys.* **2014**, *86*, 253−305.
(57) Freysoldt, C.; Neugebauer, J. First-Principles Calculations for Charged Defects at Surfaces, Interfaces, and Two-Dimensional Materials in the Presence of Electric Fields. *Phys. Rev. B: Condens. Matter Mater. Phys.* **2018**, *97*, 205425.
(58) Li, S.; Zhong, C.; Henning, A.; Sangwan, V. K.; Zhou, Q.; Liu, X.; Rahn, M. S.; Wells, S. A.; Park, H. Y.; Luxa, J.; et al. Molecular-Scale Characterization of Photoinduced Charge Separation in Mixed-Dimensional InSe-Organic van Der Waals Heterostructures. *ACS Nano* **2020**, *14*, 3509−3518.
(59) Neaton, J. B.; Hybertsen, M. S.; Louie, S. G. Renormalization of Molecular Electronic Levels at Metal-Molecule Interfaces. *Phys. Rev. Lett.* **2006**, *97*, 216405.
(60) Cho, Y.; Berkelbach, T. C. Environmentally Sensitive Theory of Electronic and Optical Transitions in Atomically Thin Semiconductors. *Phys. Rev. B: Condens. Matter Mater. Phys.* **2018**, *97*, 041409.
(61) Zhou, Q.; Liu, Z.-F.; Marks, T. J.; Darancet, P. Range-Separated Hybrid Functionals for Mixed-Dimensional Heterojunctions: Application to Phthalocyanines/$MoS_2$. *arXiv (Condensed Matter.Materials Science)*, July 22, **2021**, 2107.08516, ver. 2. https://arxiv.org/abs/2107.08516 (accessed 2021-09-05).
(62) Tkatchenko, A.; Scheffler, M. Accurate Molecular van Der Waals Interactions from Ground-State Electron Density and Free-Atom Reference Data. *Phys. Rev. Lett.* **2009**, *102*, 073005.
(63) Ling, X.; Fang, W.; Lee, Y.-H.; Araujo, P. T.; Zhang, X.; Rodriguez-Nieva, J. F.; Lin, Y.; Zhang, J.; Kong, J.; Dresselhaus, M. S. Raman Enhancement Effect on Two-Dimensional Layered Materials: Graphene, h-BN and $MoS_2$. *Nano Lett.* **2014**, *14*, 3033−3040.
(64) Hong, J.; Hu, Z.; Probert, M.; Li, K.; Lv, D.; Yang, X.; Gu, L.; Mao, N.; Feng, Q.; Xie, L.; et al. Exploring Atomic Defects in Molybdenum Disulphide Monolayers. *Nat. Commun.* **2015**, *6*, 1−8.
(65) Taghipour, N.; Martinez, P. L. H.; Ozden, A.; Olutas, M.; Dede, D.; Gungor, K.; Erdem, O.; Perkgoz, N. K.; Demir, H. V. Near-Unity Efficiency Energy Transfer from Colloidal Semiconductor Quantum Wells of CdSe/CdS Nanoplatelets to a Monolayer of $MoS_2$. *ACS Nano* **2018**, *12*, 8547−8554.
(66) Haldar, A.; Cortes, C. L.; Darancet, P.; Sharifzadeh, S. Microscopic Theory of Plasmons in Substrate-Supported Borophene. *Nano Lett.* **2020**, *20*, 2986−2992.
(67) Raja, A.; Montoya-Castillo, A.; Zultak, J.; Zhang, X. X.; Ye, Z.; Roquelet, C.; Chenet, D. A.; Van Der Zande, A. M.; Huang, P.; Jockusch, S.; et al. Energy Transfer from Quantum Dots to Graphene and MoS2: The Role of Absorption and Screening in Two-Dimensional Materials. *Nano Lett.* **2016**, *16*, 2328−2333.
(68) Pak, J.; Jang, J.; Cho, K.; Kim, T.-Y.; Kim, J.-K.; Song, Y.; Hong, W.-K.; Min, M.; Lee, H.; Lee, T. Enhancement of Photodetection Characteristics of $MoS_2$ Field Effect Transistors Using Surface Treatment with Copper Phthalocyanine. *Nanoscale* **2015**, *7*, 18780−18788.
(69) Barbara, P. F.; Meyer, T. J.; Ratner, M. A. Contemporary Issues in Electron Transfer Research. *J. Phys. Chem.* **1996**, *100*, 13148−13168.



https://doi.org/10.1021/jacs.1c07795
J. Am. Chem. Soc. 2021, 143, 17153−17161